

Cu-doped nanocomposite $Pr_2Fe_{14}B/\alpha$-Fe ribbons with high $(BH)_{max}$

Mehran Khan Alam, Shahzab Raza, Chengyong Gao(高成勇), Guangbing Han(韩广兵), and Shishou Kang(康仕寿)
Citation: Chin. Phys. B, 2024, 33 (**12**): 127504. DOI: 10.1088/1674-1056/ad8cba
Journal homepage: http://cpb.iphy.ac.cn; http://iopscience.iop.org/cpb

What follows is a list of articles you may be interested in

Sm–Co high-temperature permanent magnet materials

Shiqiang Liu(刘世强)
Chin. Phys. B, 2019, 28 (**1**): 017501. DOI: 10.1088/1674-1056/28/1/017501

Rare earth permanent magnets prepared by hot deformation process

Ren-Jie Chen(陈仁杰), Ze-Xuan Wang(王泽轩), Xu Tang(唐旭), Wen-Zong Yin(尹文宗), Chao-Xiang Jin(靳朝相), Jin-Yun Ju(剧锦云), Don Lee(李东), A-Ru Yan(闫阿儒)
Chin. Phys. B, 2018, 27 (**11**): 117504. DOI: 10.1088/1674-1056/27/11/117504

Nanocrystalline and nanocomposite permanent magnets by melt spinning technique

Chuanbing Rong(荣传兵), Baogen Shen(沈保根)
Chin. Phys. B, 2018, 27 (**11**): 117502. DOI: 10.1088/1674-1056/27/11/117502

Micromagnetism simulation on effects of soft phase size on $Nd_2Fe_{14}B/\alpha$–Fe nanocomposite magnet with soft phase imbedded in hard phase

Yu-Qing Li(李玉卿), Ming Yue(岳明), Yi Peng(彭懿), Hong-Guo Zhang(张红国)
Chin. Phys. B, 2018, 27 (**8**): 087502. DOI: 10.1088/1674-1056/27/8/087502

Anisotropic nanocomposite soft/hard multilayer magnets

Wei Liu(刘伟), Zhidong Zhang(张志东)
Chin. Phys. B, 2017, 26 (**11**): 117502. DOI: 10.1088/1674-1056/26/11/117502

Cu-doped nanocomposite $Pr_2Fe_{14}B/\alpha$-Fe ribbons with high $(BH)_{max}$

Mehran Khan Alam, Shahzab Raza, Chengyong Gao(高成勇), Guangbing Han(韩广兵)[†], and Shishou Kang(康仕寿)[‡]

School of Physics, Shandong University, Jinan 250100, *China*

(Received 22 July 2024; revised manuscript received 15 October 2024; accepted manuscript online 30 October 2024)

The melt-spun ribbons of nominal composition $Pr_9Fe_{84.2-x}B_{6.2}P_{0.3}Zr_{0.3}Cu_x$ ($x = 0$, 0.5, 1, 2) were prepared at wheel speeds of 21 m·s^{-1}, 27 m·s^{-1}, 30 m·s^{-1}, and 33 m·s^{-1}. The XRD patterns show that as the wheel speed increases, the crystallinity of the 2:14:1 hard phase decreases, while that of the α-Fe soft phase increases. The $(BH)_{max}$, remanence, and coercivity are improved from 63 kJ·m^{-3}, 0.85 T, and 515 kA·m^{-1} for the Cu-free ribbons to 171 kJ·m^{-3}, 1.08 T, and 684 kA·m^{-1} with $x = 0.5$. The high squareness ratio of $J_r/J_s \sim 0.82$ at 0.5 at.% Cu (27 m·s^{-1}) indicates strong exchange coupling due to small grain sizes of 15 nm and 30 nm for soft and hard magnetic phases, respectively. The SEM images revealed smooth morphology and uniform element distribution at 0.5 at.% Cu (27 m·s^{-1}), contributing to the high magnetic properties. The low recoil permeability (μ_{rec}) value of 5.466×10^{-4} T/kA·m^{-1} to 1.970×10^{-4} T/kA·m^{-1} confirms the strong exchange coupling with $x = 0.5$ (27 m·s^{-1}). The initial magnetization curves show that the coercivity mechanism of the Cu-free alloy evolves from the nucleation of the reverse domain to the domain wall pinning as the wheel speed increases, resulting in a high coercivity value of 818 kA·m^{-1} (33 m·s^{-1}). Conversely, for the Cu-added alloy, the coercivity mechanism changes from pinning to the nucleation of the reverse domain from low to high wheel speed.

Keywords: Cu addition, nanocomposite, magnetic properties, energy product, remanence

PACS: 75.75.–c, 75.50.Ww, 75.60.Jk, 75.75.Cd **DOI:** 10.1088/1674-1056/ad8cba

1. Introduction

The energy crisis, along with the limited fossil fuels and the hot issue of climate change around the globe, motivates the scientists to focus on renewable sources that provide sustainable energy.[1] Permanent magnets (PM) find diverse applications in electrical apparatus, green vehicles, and wind turbines.[2,3] However, costly and rare elements such as Dy (dysprosium) and Tb (terbium) have predominantly been employed in permanent magnets and should be replace by cheaper and available materials.[4] Nanocomposite permanent magnets, consisting of hard and soft magnetic phases, are in high demand due to their superior performance, thermal stability, corrosion resistance, and low production cost.[5] While the theoretical maximum energy product ($(BH)_{max}$) for nanocomposite permanent magnets is approximately 1000 kJ·m^{-3}, the experimental value falls short of this mark.[6] The oriented exchange-spring hard-soft nanocomposite magnet is a promising concept with the potential to significantly improve the record energy product.[7] This discrepancy arises due to difficulties in optimizing microstructure[8,9] and achieving strong anisotropy,[10] which are challenging requirements for nanocomposite permanent magnets. Ideal homogeneous magnetic materials that exhibit relatively well-defined magnetization behavior, whereas real two-phase composite magnets display impurities, inhomogeneities, and complex magnetization behavior.[11] In the mixture of hard and soft nanometer magnetic phases, the remanence enhancement can be achieved by the exchange coupling interaction between magnetic grains when the magnetic moment of the soft phase aligns parallel to the average direction of the easy axes of adjacent hard magnetic grains. The optimal dimension for both phases should be twice the domain wall width of the hard phase.[12] Melt spinning[13] is the main production technique for nanocomposite PM. However, due to the lower crystallization temperature of the soft α-Fe compared to the hard $Nd_2Fe_{14}B$ phase, the grain size of the soft phase tends to grow larger during the rapid cooling process, reducing the strength of exchange coupling and magnetic properties. As a result, a discrepancy occurred between the experimental and theoretical values of $(BH)_{max}$.[12] The remanence enhancement effect is the phenomenon in which inter-grain exchange interaction occurred when remanence-to-saturation ratio (J_r/J_s) greater than 0.5.[14] Therefore, the $(BH)_{max}$ value also strongly depends on the squareness (J_r/J_s) of the demagnetization curve, and a large value of J_r/J_s can result in a high energy product $(BH)_{max}$.[15]

Furthermore, element doping is recognized as an effective way to optimize the microstructure and enhance the magnetic properties.[16,17] Zirconium (Zr) is a favorable candidate for refining the grain structures and augmenting coercivity value in nanocomposite magnetic materials.[13–18] In addition, 0.1-at.% P (Phosphorous) in $Pr_{9.5}Fe_{84}B_{6.5}$ alloy can enhance the remanence and rectangularity of the demagnetization curve.[8] Alam *et al.* reported that adding P decreases the grain size of the hard $Pr_2Fe_{14}B$ phase, while Zr reduced the grain size of α-Fe in Pr–Fe–B nanocomposite ribbons.[18] Zhang *et al.* also

[†]Corresponding author. E-mail: hangb@sdu.edu.cn
[‡]Corresponding author. E-mail: skang@sdu.edu.cn

© 2024 Chinese Physical Society and IOP Publishing Ltd

reported that P-addition contributes to increased amorphous-forming ability in the $Fe_{55}Pt_{25}B_{20}$ alloy ribbon.[19]

Besides, the copper (Cu) has the potential to reduce the grain size and enhance the exchange coupling interaction among magnetic grains. Bao *et al*. reported that the values of remanence (J_r), coercive force (H_{ci}), and $(BH)_{max}$ are 1.01 T, 793.7 kA·m^{-1}, and 146 kJ·m^{-3}, respectively, in the annealed $Nd_{12.3}Fe_{81.5}Cu_{0.2}B_6$ ribbon, which are 18.4%, 36.2%, and 49% higher than those without Cu addition.[20] Adding Cu can augment the glass-forming ability[19] and increase the coercivity of the annealed $Pr_2Fe_{14}B$ ribbons.[21] Fan *et al*. demonstrated that 1 at.% Cu in $Nd_{60}Fe_{20}Al_{10}Co_{10}$ can increase the value of H_{ci} from 298 kA·m^{-1} to 321 kA·m^{-1}, which is attributed to the improved clustering of Nd–(Fe,Co) pairs in the amorphous alloy.[22] Herbst *et al*. reported 30% enhancement of H_{ci} in the 0.5-at.% Cu-doped Nd–Fe–B alloy compared to the Cu-free alloy.[23] Copper was found to concentrate at the grain boundaries, which reduces the exchange coupling effect and enhances the coercivity in the $(Nd_{0.9}Ce_{0.1})_{14}(Fe_{0.87}Co_{0.01}Cu_{0.03})_{79.5}B_{6.5}$ alloy. Moreover, the presence of Cu can facilitate Co to enrich at the grain boundaries and then enhance the remanence from 0.71 T to 0.79 T.[24] Cu doping in $Pr_{8.5}(Fe_{0.8}Co_{0.2})_{86.5}B_5$ can increase the tendency of amorphization, reduce grain sizes, and raise the remanence value from 1.03 T to 1.09 T (20 m·s^{-1}) in an annealed ribbon.[25] Copper was also observed to decrease the crystallization temperature of $Nd_9Fe_{84}B_6Nb_{0.5}Cu_{0.5}$ alloy, and promote the nucleation and growth of hard magnetic grains at lower temperature in an annealed ribbon.[26] Yang *et al*. showed that Cu addition in $Pr_8Fe_{87-x}B_5Cu_x$ enhances the *c*-axis texture of $Pr_2Fe_{14}B$ phase and facilitates the crystallization during the melt spinning process. Additionally, Cu addition was found to accelerate the cooling process and restrain the growth of α-Fe due to high-speed crystallization.[27] Hirosawa *et al*. reported that the optimal cooling rate at which the hard magnetic phase forms are slow down by the presence of copper in $Fe_3B/Nd_2Fe_{14}B$ nanocomposite alloy.[28] Hono *et al*. reported that copper atoms aggregate to create clusters before the crystallization process occurs in $Fe_{73.5}Si_{13.5}B_9Nb_3Cu_1$ alloy. These clusters act as sites for heterogeneous nucleation and facilitate the formation of primary α-Fe crystals.[29] Ping *et al*. showed that the addition of 0.2-at.% Cu in $Nd_{4.5}Fe_{77}B_{18.5}$ alloys can decrease the crystallization temperature by around 20 °C, accelerating the crystallization process.[30]

Up to now, the highest $(BH)_{max}$ value of 146 kJ·m^{-3} in Cu-doped $Nd_{12.3}Fe_{81.5}Cu_{0.2}B_6$ alloy ribbon has been reported, which is lower than the theoretical value. Further research is still needed to improve the remanence and energy product of the nanocomposite magnetic alloys. In this regard, we have investigated the effect of Cu addition on the magnetic properties in $Pr_9Fe_{84.2-x}B_{6.2}P_{0.3}Zr_{0.3}Cu_x$ ($x = 0, 0.5, 1, 2$) melt-spun ribbons, and a $(BH)_{max}$ value of 171 kJ·m^{-3} is achieved.

2. Methods

Alloy ingots weighing 20 g with a nominal composition of $Pr_9Fe_{84.2-x}B_{6.2}P_{0.3}Zr_{0.3}Cu_x$ ($x = 0$, 0.5, 1, 2), were prepared through electric arc furnace under an argon atmosphere. The raw materials, namely praseodymium (Pr), iron (Fe), copper (Cu), zirconium (Zr), phosphorous (P), and boron (B) in the form of FeB (with 22-wt% B) with the purity of 99.5%, were employed in the proces. To offset the loss of Pr due to evaporation during melting, an additional 5-wt% Pr was introduced. The ingots underwent three successive re-melting cycles for uniformity and then were subjected to the removal of oxidized surfaces using either a grinder machine or sandpaper before being broken into smaller pieces. These broken pieces weighing approximately 8 g were placed into a quartz tube featuring a circular opening ($\sim$ 1 mm in diameter). Ribbons with a width of 0.2 mm–0.3 mm and a length of 4 mm–5 mm were produced using a melt-spinning machine under an argon atmosphere with 99.99% purity from 21 m·s^{-1} to 33 m·s^{-1}. The phase composition of the as-spun ribbons was checked by x-ray diffraction (XRD, Smartlab-se) with Cu $K\alpha$ radiation. Magnetic properties were assessed using both a vibrating sample magnetometer (VSM) with a 1.5-T magnetic field and superconducting quantum interference device (SQUID) with a 2-T magnetic field along the ribbons' long axis. Surface morphology and microstructure were investigated using scanning electron microscopy (SEM) and high-resolution transmission electron microscopy (HRTEM), respectively.

3. Results and discussion

Figure 1 gives the x-ray diffraction (XRD) patterns of $Pr_9Fe_{84.2-x}B_{6.2}P_{0.3}Zr_{0.3}Cu_x$ ($x = 0, 0.5, 1, 2$) ribbons prepared at 21 m·s^{-1}, 27 m·s^{-1}, and 33 m·s^{-1} wheel speeds. The XRD results verify the presence of three phases: α-Fe ($Im\text{-}3m$), $Pr_2Fe_{14}B$ (P_{42}/mnm), and an amorphous phase in all ribbons.

The XRD patterns for $x = 0$ (Fig. 1(a)) indicate that as the quenching speed increases from 21 m·s^{-1} to 33 m·s^{-1}, the diffraction peak of $Pr_2Fe_{14}B$ and α-Fe become wide. Peak broadening is correlated with the reduction in crystallite grain size resulting from rapid solidification during quenching. The average grain sizes, calculated by the Scherrer equation,[31] are 35 nm (21 m·s^{-1}), 25 nm (27 m·s^{-1}), and 23 nm (33 m·s^{-1}) for the $Pr_2Fe_{14}B$ phase, and 33 nm (21 m·s^{-1}), 20 nm (27 m·s^{-1}), and 17 nm (33 m·s^{-1}) for α-Fe. These findings suggest that high wheel speed decreases grain size, which is consistent with the results of Mendoza-Suárez *et al*.[32] The grain size ratio (s/h) of the soft to hard magnetic phase decreases with the increasing quenching speed, which

are 0.94 (21 m·s^{-1}), 0.80 (27 m·s^{-1}), and 0.73 (33 m·s^{-1}). The rapid cooling associated with high quenching speed preferentially facilitates the formation of hard magnetic phases over their soft counterparts. The interplay among various phases during solidification can change the relative abundance of soft and hard magnetic components. Moreover, when $x = 0$, as the quenching speed increases, the ability to form amorphous phase becomes stronger.

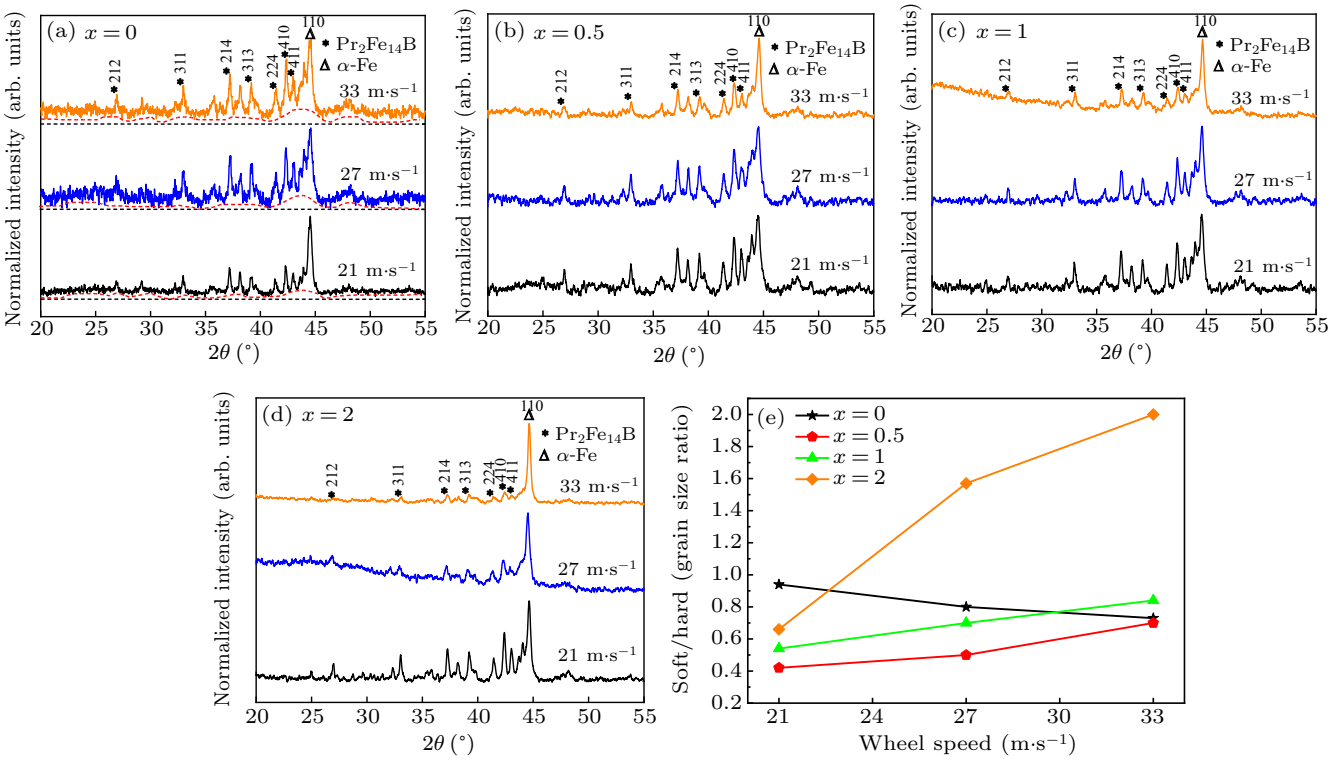


Fig. 1. XRD patterns of $Pr_9Fe_{84.2-x}B_{6.2}P_{0.3}Zr_{0.3}Cu_x$ ($x = 0$, 0.5, 1, 2) ($x = 0$ (a), 0.5 (b), 1 (c), 2 (d)) ribbons prepared at wheel speeds of 21 m·s^{-1}, 27 m·s^{-1}, 33 m·s^{-1} with corresponding (e) grain size ratio of soft to hard magnetic phase (s/h).

With the addition of 0.5-at.% Cu, the grain size at 21 m·s^{-1} is reduced compared Cu-free, from 35 nm to 33 nm for the $Pr_2Fe_{14}B$, and from 33 nm to 14 nm for the α-Fe. However, further increasing the wheel speed results in the grain size growth of the soft phase, while that of the hard phase is suppressed. The grain sizes are 33 nm (21 m·s^{-1}), 30 nm (27 m·s^{-1}), 24 nm (33 m·s^{-1}) for the hard phase, and 14 nm (21 m·s^{-1}), 15 nm (27 m·s^{-1}), 17 nm (33 m·s^{-1}) for the soft phase, respectively. The s/h values for $x = 0.5$ are 0.42 (21 m·s^{-1}), 0.50 (27 m·s^{-1}), and 0.70 (33 m·s^{-1}).

Similarly, for $x = 1$, the grain sizes are 22 nm (21 m·s^{-1}), 20 nm (27 m·s^{-1}), 19 nm (33 m·s^{-1}) for the hard phase, and 12 nm (21 m·s^{-1}), 14 nm (27 m·s^{-1}), 16 nm (33 m·s^{-1}) for the soft phase, respectively. The s/h values are 0.54 (21 m·s^{-1}), 0.70 (27 m·s^{-1}), and 0.84 (33 m·s^{-1}). A similar trend is observed in the ribbons with $x = 2$. It is evident that in Cu-doped alloys, as the quenching speed increases, the relative grain size of the hard phase decreases, while that of the soft phase increases.

Throughout the XRD patterns, it is observed that with the increase in wheel speed, the peak of the soft phase becomes more pronounced in the Cu-doped alloy. This indicates that the crystallization temperature of the soft phase is higher than that of Cu-free alloy. Higher crystallization temperature typically results in larger grain sizes and enhanced crystallinity. Subsequently, the relative crystallinity of the hard phase[33] decreases with the increasing wheel speed, while that of the soft phase increases slightly.

Figure 2 displays the hysteresis loops of the as-spun ribbons. The hysteresis loop for $x = 0$ (21 m·s^{-1}) is narrow and exhibits a high saturation magnetization of 1.43 T and low coercivity of 234 kA·m^{-1}. As the wheel speed increases, the coercivity improves to 515 kA·m^{-1} (27 m·s^{-1}), 538 kA·m^{-1} (30 m·s^{-1}), and 818 kA·m^{-1} (33 m·s^{-1}), but the remanence declines from 0.88 T (21 m·s^{-1}) to 0.81 T (33 m·s^{-1}).

All the hysteresis loops exhibit a noticeable kink, which means that some of the large soft magnetic grains are partially or entirely disconnected from the surrounding grains and revere independently.[34,35] This is supported by the XRD patterns in Fig. 1(a), which show that a large amorphous region is introduced between the grains, particularly in the ribbon prepared at the speed of 33 m·s^{-1}. This produces a decoupling effect and significantly enhances the coercivity.[36]

The loops in Fig. 2(b) ($x = 0.5$) show the single-phase magnetic characteristic without any kink. The coercivity is enhanced from 234 kA·m^{-1} (Cu-free) to 727 kA·m^{-1} in the

ribbons with $x = 0.5$ prepared at wheel speed of 21 m·s^{-1} and then drops to 559 kA·m^{-1} ($x = 0.5$) at the speed of 33 m·s^{-1}. This is due to the decrease of the crystallinity of the hard phase at high wheel speed. The remanence improved from 0.88 T to 0.99 T with the addition of 0.5-at.% Cu in the ribbon prepared at the speed of 21 m·s^{-1}, increased further to 1.08 T (27 m·s^{-1}) and then dropped to 1.01 T (30 m·s^{-1}) and 0.95 T (33 m·s^{-1}). The ratio of J_r/J_s increases from 0.71 (21 m·s^{-1}) to 0.82 (27 m·s^{-1}) and subsequently reduces to 0.78 (30 m·s^{-1}) and 0.75 (33 m·s^{-1}) for the ribbon with $x = 0.5$. This implies that the strength of remanence enhancement in the ribbons can be controlled by Cu addition and wheel speed.[24] The high J_r/J_s value of 0.82 in the ribbon wit $x = 0.5$ (27 m·s^{-1}) can be attributed to the strong exchange coupling between the hard and soft magnetic grains,[37] which are 30 nm and 15 nm, respectively, with s/h ratio of 0.50.

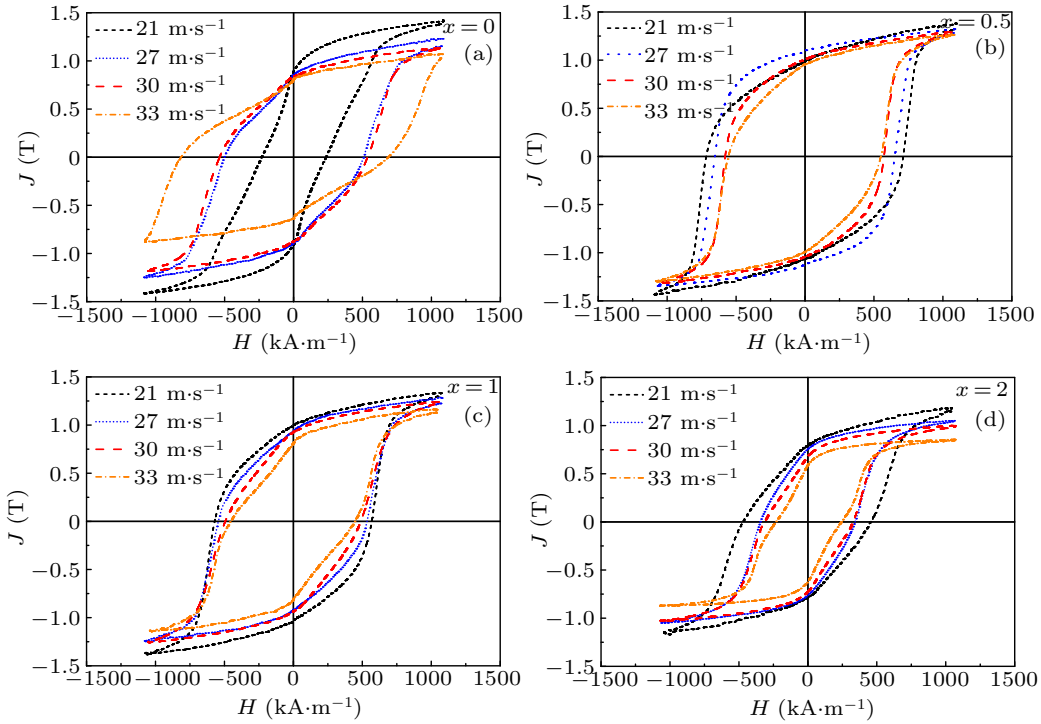


Fig. 2. Magnetic hysteresis loops for $Pr_9Fe_{84.2-x}B_{6.2}P_{0.3}Zr_{0.3}Cu_x$ ($x = 0$ (a), 0.5 (b), 1 (c), 2 (d)) ribbons prepared at different wheel speeds.

Figure 2(c) ($x = 1$) shows that the coercivity and remanence decline with increase in wheel speed. The coercivity values are 574 kA·m^{-1} (21 m·s^{-1}), 551 kA·m^{-1} (27 m·s^{-1}), 502 kA·m^{-1} (30 m·s^{-1}), and 463 kA·m^{-1} (33 m·s^{-1}). The remanence values are 1.0 T (21 m·s^{-1}), 0.94 T (27 m·s^{-1}), 0.92 T (30 m·s^{-1}), and 0.81 T (33 m·s^{-1}). The corresponding soft-to-hard grain size ratios are 0.54 (21 m·s^{-1}), 0.70 (27 m·s^{-1}), and 0.84 (33 m·s^{-1}), respectively. It is obvious that the magnetic properties are strongly correlated to the soft-to-hard grain size ratio.

For $x = 2$, the coercivity values vary from 472 kA·m^{-1} (21 m·s^{-1}) to 237 kA·m^{-1} (33 m·s^{-1}) and, the remanence is from 0.80 T (21 m·s^{-1}) to 0.59 T (33 m·s^{-1}). The ribbons fabricated at the speed of 33 m·s^{-1} have the grain size of about 12 nm for the hard phase, whereas that of the soft grain is about 24 nm (Fig. 1(d) ($x = 2$)). The s/h value is approximately 2.0, which is relatively large and deteriorates the magnetic properties.

Figure 3 shows the dependence of (a) $(BH)_{max}$ values and (b) J_r/J_s on the wheel speed. For $x = 0$, as the wheel speed changes from 21 m·s^{-1} to 33 m·s^{-1}, the $(BH)_{max}$ increases from 33 kJ·m^{-3} to 72 kJ·m^{-3}, and the value of J_r/J_s increases from 0.62 to 0.75 (Fig. 3(b)). For $x = 0.5$, the $(BH)_{max}$ value initially increases from 123 kJ·m^{-3} (21 m·s^{-1}) to 171 kJ·m^{-3} (27 m·s^{-1}) and subsequently reduces to 126 kJ·m^{-3} (30 m·s^{-1}) and 95 kJ·m^{-3} (33 m·s^{-1}). Similarly, the ratio of J_r/J_s also increases from 0.71 (21 m·s^{-1}) to 0.82 (27 m·s^{-1}) and then drops to 0.78 (30 m·s^{-1}) and 0.75 (33 m·s^{-1}). The high $(BH)_{max}$ value of 171 kJ·m^{-3} (27 m·s^{-1}) for $x = 0.5$ may come from the robust exchange coupling between hard and soft magnetic grain, as evidenced by the highest J_r/J_s ratio of 0.82, where the soft-to-hard grain size ratio is 0.5, which is consistent with Suárez's report.[32] Maintaining a grain size of 30 nm for $Pr_2Fe_{14}B$ and 15 nm for α-Fe in the ribbon with $x = 0.5$ (27 m·s^{-1}) results in the s/h value of 0.5. This ratio can lead to a high J_r/J_s value of 0.82 and subsequently a high $(BH)_{max}$ value of 171 kJ·m^{-3}. This $(BH)_{max}$ value is the highest reported so far in the nanocomposite magnetic alloy with a rare earth content of 9.0 at.%.

With the addition of 1 at.% Cu, the $(BH)_{max}$ value decreases from 110 kJ·m^{-3} (21 m·s^{-1}) to 54 kJ·m^{-3} (33 m·s^{-1}) with J_r/J_s values of 0.75 and 0.69, respectively. Similarly, for

$x = 2$, the $(BH)_{max}$ value decreases from 62 kJ·m^{-3} (21 m·s^{-1}) to 21 kJ·m^{-3} (33 m·s^{-1}). The value of J_r/J_s decreases progressively with the increase of s/h from 0.66 to 2.0. Hence, the high Cu content and wheel speed significantly increase the value of s/h and decreases the value of $(BH)_{max}$ value.

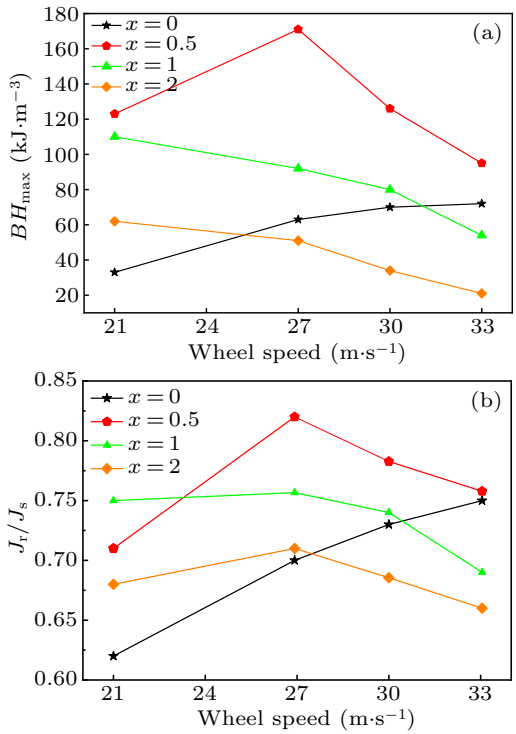


Fig. 3. The dependence of $(BH)_{max}$ (a) and remanence to saturation ratio (J_r/J_s) (b) on the wheel speed for $Pr_9Fe_{84.2-x}B_{6.2}P_{0.3}Zr_{0.3}Cu_x$ ($x = 0$, 0.5, 1, 2) ribbons.

Figure 4 presents surface SEM images and corresponding elemental mapping of the ribbons prepared at wheel speed of 27 m·s^{-1}. The SEM image for $x = 0$ reveals a non-uniform microstructure with cracks and scratches where the Fe content is very low, as shown by the elemental mapping (Fig. 4(a)). Conversely, the SEM image for $x = 0.5$ displays a smooth and uniform surface, with corresponding elemental mapping showing an even distribution of elements. For $x = 0$, a large number of gas pockets[38] are found, which is fewer in the ribbon with $x = 0.5$. Cu addition promotes a uniform elemental distribution, which is beneficial for strong exchange coupling between magnetic grains. Figure 4(c) shows the well-defined layered and elongated grain microstructure in the ribbons with 2-at.% Cu. The elemental mapping of the Fe shows that the layers come from the alignment of Fe-rich grains. However, the other elements are evenly distributed. These layers may contribute to the large grain size of the iron in the XRD pattern, which exhibits a high and narrow peak of Fe, as shown in Fig. 1(d) (2-at.% Cu).

Figure 5 shows the HRTEM images of the ribbon with ($x = 0$ (a) and 0.5 (b)) prepared at the wheel speed of 27 m·s^{-1}. The images show obvious lattice spacing reflecting the soft α-Fe, hard 2:14:1 and amorphous phases. For $x = 0$, the average grain size is 29 nm for the hard phase and 23 nm for the soft phase, resulting in an s/h ratio of 0.79, which closely matches the XRD result of 0.8. Similarly, for $x = 0.5$, the average grain sizes are 14 nm for the soft phase and 28 nm for the hard phase, yielding a ratio of 0.5. The s/h ratio of 0.5 is the main reason for the high $(BH)_{max}$ value of 171 kJ·m^{-3} ($x = 0.5$) compared to 63 kJ·m^{-3} ($x = 0$) at 27 m·s^{-1}. This ratio is particularly favorable for strong exchange coupling interaction, which enhances the energy product value.

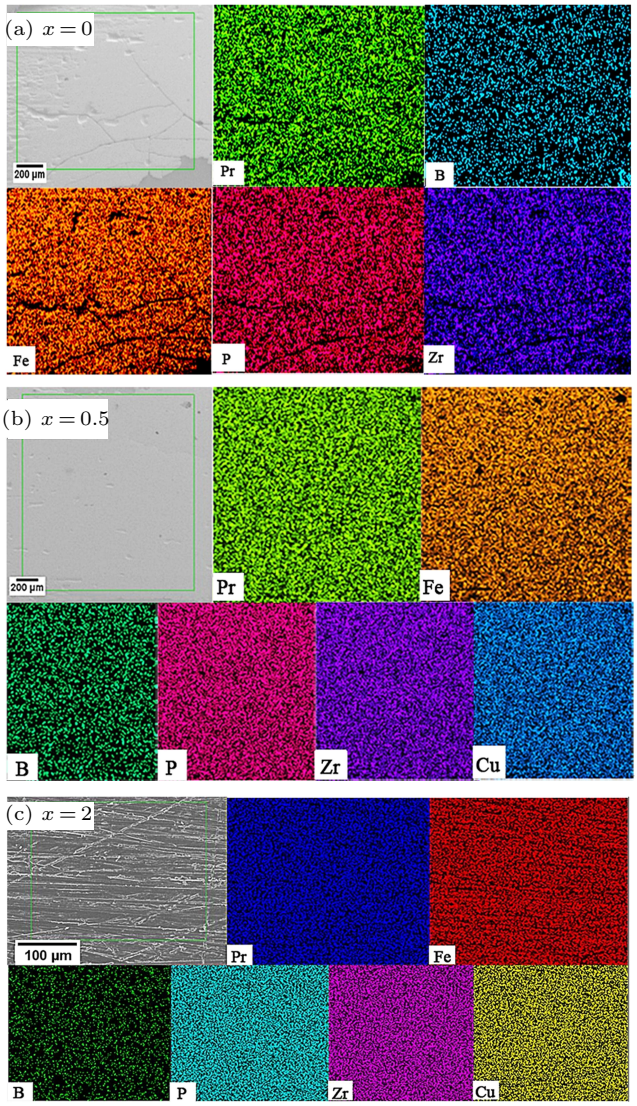


Fig. 4. Surface SEM images for $Pr_9Fe_{84.2-x}B_{6.2}P_{0.3}Zr_{0.3}Cu_x$ ($x = 0$ (a), 0.5 (b), 2 (c)) ribbons quenched at wheel speeds of 27 m·s^{-1}, and the corresponding elemental mappings.

Table 1 depicts the lattice constants and cell volume of the $Pr_2Fe_{14}B$ phase, which were derived from the XRD pattern data. The introduction of copper resulted in a reduction of crystal lattice constants, consequently shrinking the volume of the unit cell.[39] The decrease in unit cell volume indicates that Cu atoms likely integrate into the 2:14:1 phase. With the atomic radii of 0.128 nm for Cu, 0.187 nm for Pr, 0.124 nm for Fe, and 0.087 nm for B, it is reasonable to propose that Cu atoms may occupy lattice sites originally held

by Pr atoms. Additionally, some copper atoms accumulate at grain boundaries,[40] contributing to a refined microstructure, and reducing the grain size of the hard 2:14:1 phase, as illustrated by the XRD pattern in Fig. 1 for the Cu-doped sample.

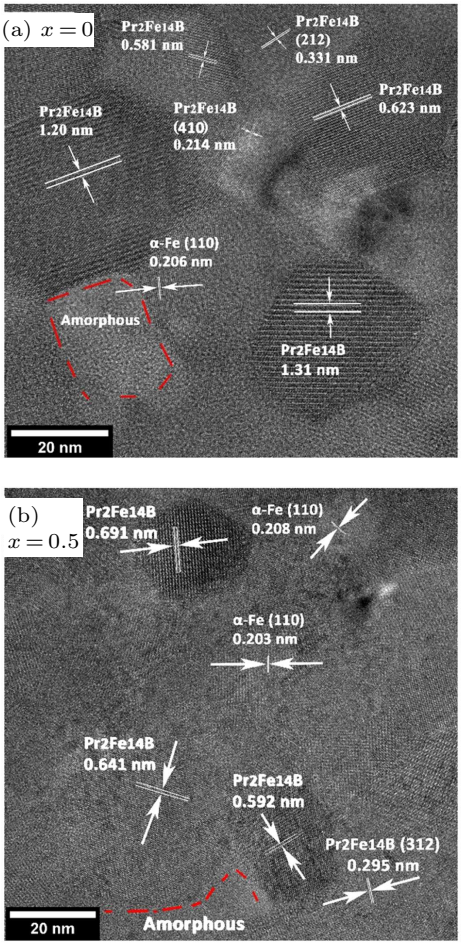


Fig. 5. HRTEM images for $Pr_9Fe_{84.2-x}B_{6.2}P_{0.3}Zr_{0.3}Cu_x$ ($x = 0$ (a) and 0.5 (b)) ribbons quenched at wheel speeds of 27 m·s^{-1}.

Table 1. The lattice constants and cell volume of 2:14:1 phase for the $Pr_9Fe_{84.2-x}B_{6.2}P_{0.3}Zr_{0.3}Cu_x$ ($x = 0$–2) ribbons prepared at 27 m·s^{-1}.

Composition	a (Å)	c (Å)	V (Å)^3
$x = 0$	8.802	12.209	946.11
$x = 0.5$	8.798	12.201	944.49
$x = 1$	8.797	12.197	944.09
$x = 2$	8.787	12.172	939.81

The role of magnetic interaction and its nature can be evaluated with the recoil permeability μ_{rec} which is represented by the slopes of the recoil loops. Figure 6 gives the recoil loop curves of the $Pr_9Fe_{84.2-x}B_{6.2}P_{0.3}Zr_{0.3}Cu_x$ ($x = 0$, 0.5, 1, 2) ribbons prepared at 27 m·s^{-1}. In Fig. 6 ($x = 0$), the recoil loop gives the μ_{rec} values that range from 1.150×10^{-3} T/kA·m^{-1} to 2.027×10^{-4} T/kA·m^{-1} from low to high magnetic field. Upon introducing 0.5-at.% Cu, the values of μ_{rec} range from 5.466×10^{-4} T/kA·m^{-1} to 1.970×10^{-4} T/kA·m^{-1} with the increase of the external field. The low permeability values in the Cu-doped ribbon suggest strong exchange coupling among magnetic grains, resulting in the concurrent reversal of soft and hard phases.[39] The spontaneous switching of both magnetic grains results in high magnetic properties, with H_c of 684 kA·m^{-1}, J_r of 1.088 T, $(BH)_{max}$ of 171 kJ·m^{-3}. For $x = 1$, the μ_{rec} ranges from 1.058×10^{-3} T/kA·m^{-1} to 2.243×10^{-4} T/kA·m^{-1} which is slightly higher than that of $x = 0.5$, indicating the existence of two phases that reverse independently at lower field.[41] Finally, for $x = 2$, the value range of μ_{rec} increases from 3.200×10^{-3} T/kA·m^{-1} to 2.842×10^{-4} T/kA·m^{-1}, which suggests a relatively weak exchange coupling interaction, as confirmed by the hysteresis loops in Fig. 2(d). The increase in recoil permeability value with Cu-doping is attributed to the grain growth of the soft phase relative to the hard phase, as demonstrated by the XRD patterns in Fig. 1 (27 m·s^{-1}).[42]

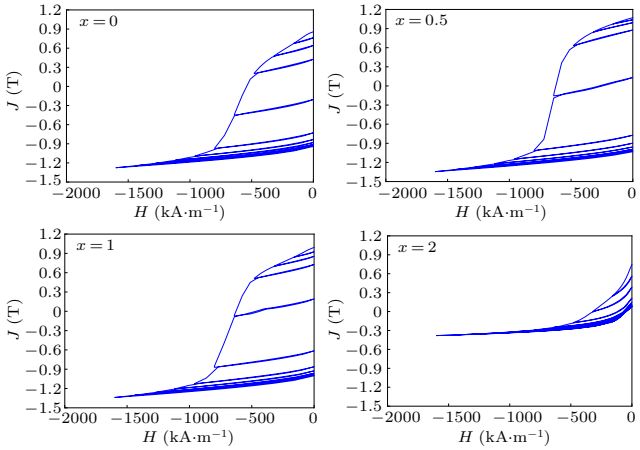


Fig. 6. Recoil loops for $Pr_9Fe_{84.2-x}B_{6.2}P_{0.3}Zr_{0.3}Cu_x$ ($x = 0$, 0.5, 1, 2) ribbons at wheel speeds of 27 m·s^{-1}.

Figure 7 represents the initial magnetization curve for the $Pr_9Fe_{84.2-x}B_{6.2}P_{0.3}Zr_{0.3}Cu_x$ ($x = 0$, 0.5, 1, 2) alloy ribbon prepared at wheel speed ranging from 21 m·s^{-1} to 33 m·s^{-1}. For $x = 0$, the initial magnetization behavior indicates that the coercivity mechanism of the ribbon prepared at 21 m·s^{-1} is based on the nucleation of reverse domain. The initial curve bends slightly at the wheel speed of 27 m·s^{-1} and shows a steeper incline at the speed of 30 m·s^{-1}, indicating that the strength of domain wall pinning increases with the wheel speed. For the wheel speed of 33 m·s^{-1}, the initial curve shows the coercivity is dominantly controlled by domain wall pinning,[43] and the high coercivity value of 818 kA·m^{-1} is achieved. It can be seen from Fig. 1(a) that the amorphous content increases with quenching speed. The intergranular amorphous layers between the nanocrystals prevent domain walls from moving. Domain walls are interfaces separating distinct magnetic domains, and their movement is essential for magnetization and demagnetization processes. When amorphous layers are encountered, these domain walls become "pinned" or obstructed

in their movement.[44] Coercivity refers to a magnetic substance's resistance to demagnetization. The presence of these amorphous layers enhances the material's coercivity. As a result, the pinning centers (amorphous layers) inhibit domain wall movement, requiring a stronger external magnetic field to realign the magnetic domains.

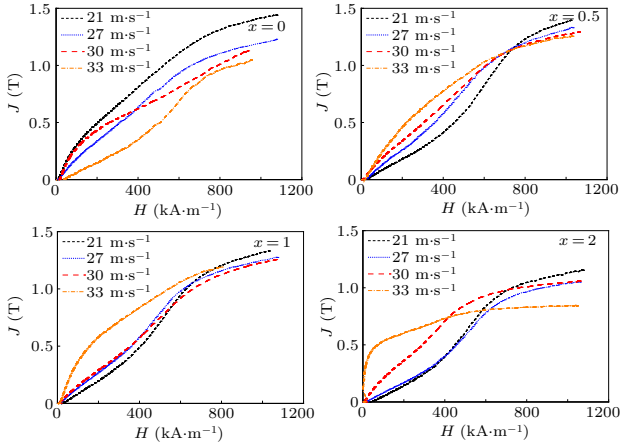


Fig. 7. Initial magnetization curves for $Pr_9Fe_{84.2-x}B_{6.2}P_{0.3}Zr_{0.3}Cu_x$ ($x = 0$, 0.5, 1, 2) ribbons prepared at wheel speeds of 21 m·s^{-1} to 33 m·s^{-1}.

For $x = 0.5$, the initial curve shows the pinning mechanism for the coercivity in the ribbon prepared at 21 m·s^{-1}. As the wheel speed increases, the coercivity mechanism changes from dominant domain wall pinning to the combination of pinning and nucleation, eventually becoming a dominant nucleation mechanism of the reverse domain. A similar trend is also observed with $x = 1$. Figure 7 ($x = 2$) indicates that the coercivity mechanism is the pinning of the domain wall for the ribbons prepared at 21 m·s^{-1} and 27 m·s^{-1}, and then shifts slightly towards nucleation of the reverse domain at 30 m·s^{-1} and 33 m·s^{-1}. This can be attributed to the higher content of soft α-Fe phase in the ribbons prepared at higher wheel speed.

4. Conclusion

The ribbons of $Pr_9Fe_{84.2-x}B_{6.2}P_{0.3}Zr_{0.3}Cu_x$ ($x = 0$, 0.5, 1, 2) were obtained by melt spinning at the wheel speeds of 21 m·s^{-1}, 27 m·s^{-1}, 30 m·s^{-1}, and 33 m·s^{-1}, respectively. XRD analysis revealed that the Cu-doping decreases the crystallinity of the 2:14:1 phase and increases that of the soft α-Fe phase. Significant improvements in magnetic properties were achieved with the addition of 0.5-at.% Cu, including the remanence (J_r) and intrinsic coercivity (H_c). The highest $(BH)_{max}$ value of 171 kJ·m^{-3} was achieved in the ribbon with $x = 0.5$ prepared at the wheel speed of 27 m·s^{-1} due to the strong exchange coupling between hard and soft magnetic grains, with the grain size ratio (s/h, soft-to-hard phase) of 0.5. The SEM analysis reveals a uniform distribution of elements and smooth morphology, contributing to the superior magnetic properties in the 0.5-at.% Cu-doped alloy prepared at speed of 27 m·s^{-1}. The coercivity mechanism changes with the increase in wheel speed; it shifts from the nucleation of the reverse domain to the pinning of the domain wall in Cu-free ribbons, while in Cu-doped ribbons, it changes from pinning to nucleation.

Acknowledgements

Project supported by the National Natural Science Foundation of China (Grant Nos. 12074220 and 11627805) and the National Key Research and Development Program of China (Grant No. 2023YFA1406604). We extend our appreciation to Song and Zheng from ZKKF (Beijing), as well as Kuai from Core Facility Sharing Platform of Shandong University, for their valuable assistance in TEM and XRD support, respectively.

References

[1] Gutfleisch O, Willard MA, Brück E, Chen C H, Sankar S G and Liu J P 2011 *Adv. Mater.* **23** 821
[2] Szmaja W, Grobelny J, Cichomski M, Hirosawa S and Shigemoto Y 2011 *Acta Mater.* **59** 531
[3] Li Y, Fan X, Jia Z, Fan L, Ding G, Liu X, Guo S, Zheng B, Cao S, Chen R and Yan A 2024 *Chin. Phys. B* **33** 037508
[4] Liu Z, He J and Ramanujan R V 2021 *Mater. Des.* **209** 110004
[5] Mican S, Hirian R, Isnard O, Chicinaş I and Pop V 2015 *Phys. Procedia* **75** 1314
[6] Hewei D, Chunxiang C, Wei Y and Jibing S 2017 *J. Rare Earths* **35** 468
[7] Coey J M D 2020 *J. Eng.* **6** 119
[8] Wang L, Quan Q, Zhang L, Hu X, Rehman S, Jiang Q, Du J and Zhong J 2018 *Appl. Phys.* **123** 113904
[9] Yang Z, Chen Y, Liu W, Li Y, Cong L, Wu Q, Zhang H, Lu Q, Zhang D and Yue M 2023 *Chin. Phys. B* **32** 047504
[10] Zeng X R, Sheng H C, Jin C X and Qian H X 2016 *J. Magn. Magn. Mater.* **401** 1155
[11] Herbst J F 1991 *Rev. Mod. Phys.* **63** 819
[12] Yang S, Liu X, Li S, Qin W, Song X, Lu M and Du Y 2003 *J. Alloys Compd.* **358** 316
[13] Goll D and Kronmüller H 2000 *Sci. Nat.* **87** 423
[14] Rong C and Shen B 2011 *Chin. Phys. B* **27** 117502
[15] Kanekiyo H, Uehara M and Hirosawa S 1993 *IEEE Tran. Magn.* **29** 2863
[16] Zhang W Y, Kharel P, Al-Omari I A, Shield J E and Sellmyer D J 2016 *Phil. Mag.* **96** 2800
[17] Wang C Z, Liu L, Sun Y L, Zhao J T, Zhou B, Tu S S, Wang C G, Ding Y and Yan A R 2023 *Chin. Phys. B* **32** 020704
[18] Alam M K, Han G B and Kang S S 2021 *J. Magn. Magn. Mater.* **517** 167345
[19] Zhang W, Kazahari A, Yubuta K, Makino A, Wang Y, Umetsu R and Li Y 2014 *J. Alloys Compd.* **586** 294
[20] Bao X, Gao X, Zhang M, Qiao Y, Guo X, Zhu J and Zhou S 2008 *J. Uni. Sci. Tech. Beijing Mineral. Met. Mater.* **15** 753
[21] Withanawasam L, Zhang Y J and Hadjipanayis G C 1991 *J. Appl. Phys.* **70** 6450
[22] Fan GJ, Löser W, Roth S, Eckert J and Schultz L 1991 *Appl. Phys. Lett.* **75** 2984
[23] Herbst J F, Fuerst C D, Mishra R K, Murphy C B and Wingerden D J V 1991 *J. Appl. Phys.* **69** 5823
[24] Munan Y, Shuwei Z, Yaojun L, Chunming W, Jiajie L and Bin Y 2018 *Mater. Res. Express* **6** 026534
[25] Wang Z, Zhang M, Zhou S, Qiao Y and Wang R 2000 *J. Alloys Compd.* **309** 212
[26] Salazar D, Martín-Cid A, Madugundo R, Garitaonandia J S, Barandiaran J M and Hadjipanayis G C 2006 *J. Appl. Phys D: Appl. Phys.* **50** 015305

[27] Yang B, Shen B G, Zhao T Y and Sun J R 2007 *Mater. Sci. Eng: B* **145** 11

[28] Hirosawa S, Shigemoto Y, Miyoshi T and Kanekiyo H 2003 *Scr. Mater.* **48** 839

[29] Hono K, Ping D H, Ohnuma M and Onodera H 1991 *Acta Mater.* **47** 997

[30] Ping D H, Hono K, Kanekiyo H and Hirosawa S 1991 *Acta Mater.* **47** 4641

[31] Patterson A L 1939 *Phys. Rev.* **56** 978

[32] Suárez G M, Garcıa J I E, Cuevas J L, Gutiérrez G V, Molinar H M and Nonell J M 1999 *J. Magn. Magn. Mater.* **206** 37

[33] Hirosawa S, Kanekiyo H, Shigemoto Y, Murakami K, Miyoshi T and Shioya Y 2002 *J. Magn. Magn. Mater.* **239** 424

[34] Wang Z, Zhou S, Zhang M, Qiao Y and Wang R 1999 *J. Appl. Phys.* **86** 7010

[35] Li A H, Chiu C H, Chnag H W, Chang W C and Li W 2007 *J. Alloys Compd.* **437** 197

[36] Alam M K, Raza S, Han G B and Kang S S 2023 *Phys. Status Solidi (a)* **220** 2200656

[37] Wang L, Wang J, Rong M, Rao G and Zhou H 2018 *J. Rare Earths* **36** 1179

[38] Poenaru I, Lixandru A, Riegg S, Fayyazi B, Taubel A, Güth K, Gauß R and Gutfleisch O 2019 *J. Magn. Magn. Mater.* **478** 198

[39] Alam M K, Han G B and Kang S S 2020 *Rare Metals* **39** 41

[40] Herbst J F, Fuerst C D, Mishra R K, Murphy C B and Wingerden D J V 1991 *J. Appl. Phys.* **69** 5823

[41] Goll D, Seeger M and Kronmüller H 1998 *J. Magn. Magn. Mater.* **185** 49

[42] Panagiotopoulos I, Withanawasam L and Hadjipanayis G C 1996 *J. Magn. Magn. Mater.* **152** 353

[43] Alam M K, Raza S, Han G B and Kang 2024 *Phys. Status Solidi (a)* **221** 2300626

[44] Zhang Y, Li W, Li H and Zhang X 2013 *J. Phys. D: Appl. Phys.* **47** 015002